RESEARCH ARTICLE

Electromechanical Evaluation of a Double-Core Motor With Ceramic Elements

OLEKSANDR DOBZHANSKYI[1], **RUPERT GOUWS**[2], **(Member, IEEE), KEVIN BENNION**[3],
BIDZINA KEKELIA[3], **(Member, IEEE), J. TOMERLIN**[3], **E. COUSINEAU**[3], **(Member, IEEE),
AND SREEKANT NARUMANCHI**[3], **(Senior Member, IEEE)**

[1]Department of Natural Science, Engineering, and Technology, Point Park University, Pittsburgh, PA 15209, USA
[2]School of Electrical, Electronic and Computer Engineering, North-West University, Potchefstroom 2520, South Africa
[3]National Renewable Energy Laboratory, Golden, CO 80401, USA

Corresponding author: Oleksandr Dobzhanskyi (odobz@pointpark.edu)

ABSTRACT This study investigated the prospect of embedding ceramic elements in the body of a double-core transverse-flux machine to mitigate heat in the machine's coil. In addition, the ceramic elements were used to hold the coil above the permanent magnets in order to reduce the negative flux leakage of the magnets into the coil. Three types of ceramics were investigated for this purpose: glass ceramic, aluminum oxide, and silicon nitride. Steady-state thermal analysis demonstrated a significant temperature drop in the motor coil when the ceramic element was embedded in the design. The back electromotive force of the winding improved by 30% as a result of reduced leakage flux. Structural analysis of the motor demonstrated high endurance of the ceramic elements to thermal stress and motor vibration. The results of computer thermal analysis were verified in the laboratory by performing a test on a section of a motor.

INDEX TERMS Ceramic element, thermal stress, transverse-flux motor, vibration analysis.

I. INTRODUCTION

Modern low-speed propulsion systems require compact high-torque-density permanent-magnet (PM) electric motors. By combining two stators with a mutual PM rotor between each stator, the power density of an electric motor can be greatly improved [1], [2], [3]. On the other hand, effective cooling strategies are necessary to eliminate excessive heat from such machines. Despite the numerous papers on the machines with two stators [3], [4], [5], [6], [7], [8], [9], [10], [11], [12] there is still a gap in developing effective cooling strategies of these machines. In most cases, the discussion on double-core motors, including transverse-flux machines (TFM) [13], [14], [15], is limited to electromagnetic analysis, where the thermal and structural models of these machines are not studied in detail. The paper aims to embed ceramic element in the TFM motor to improve heat transfer from

the motor coil to the machine rotor. The importance of this innovative approach can develop a platform of using ceramic in motor housing, and cooling jackets instead of aluminum and other metals. The other goal of the research is to use the ceramic elements to suspend the motor coil above the PMs to limit the leakage flux. In order to confirm the effectiveness of the new design with ceramic elements, this study merges electromagnetic, thermal, structural, and acoustic analysis.

To reduce the total cost and simplify manufacturing process of the machine, two lightweight inexpensive ceramic elements are used in the design.

In TFMs these magnets are situated between the stator poles at a particular instant. The flux produced by the inactive magnets links the coil between the stator poles with the opposite (negative) direction as it is in the stator core. Therefore, the flux linkage of the coil decreases which impacts the performance of the machine [16]. Placing the coil above the PMs reduces the negative flux, which results in higher back electromotive force (EMF) in the motor [17], [18]. The

The associate editor coordinating the review of this manuscript and approving it for publication was Jenny Mahoney.

coil suspension above the PMs is a novelty of this design. In conventional TFMs the coil is usually placed on the rotor disc on the same level as PMs.

The use of ceramic elements in electrical motors is not fully researched. Some efforts have been made to develop ceramic insulators for the winding [19], [20], but these studies didn't address the thermal and structural capabilities of the ceramic materials when applied to electrical machines. This paper investigates the feasibility of using ceramic elements as part of an electrical machine by conducting a detailed structural analysis in 3D finite element method (FEM) and investigating the influence of the motor temperature and vibration on the machine's elements. The main motivation of the research is that the discussion of motor winding cooling by the ceramic elements is missed from the literature, and requires further investigation [21].

In the proposed design, expensive rare-earth PMs are replaced by affordable ferrite magnets (FMs) which are widely available in the United States. The scarcity of rare-earth elements in the United States has become both a commercial bottleneck and a national security problem. The importing of material from countries outside the United States has become increasingly difficult and expensive. The motivation of this work is to seek alternative rare-earth-material-free sources of motor excitation leading to the exploration of FMs in this study. The advantages of the FMs compared to the rare-earth magnets include: (1) significantly lower cost, especially when manufactured in large volumes; (2) higher demagnetizing temperatures; and (3) resistance to corrosion. Another advantage of the FMs is negligible electrical conductivity which eliminates heat generation in the FMs. The high operating temperature of the FMs allows coil heat transfer to the PMs through the ceramic element. As a result, the coil temperature drops which allows the motor to operate at higher load conditions.

In order to eliminate rotor core losses and improve the efficiency of the TFM, the conventional iron core is replaced by non-magnetic steel 904L.

II. ELECTROMAGNETIC ANALYSIS

The transverse-flux machine with double core is illustrated in Fig. 1.

The rotor of the machine is made of two rows of PMs firmly attached to both sides of the rotor disc (Fig. 1 b). The active magnets are facing stator poles at a particular instant, whereas the inactive magnets at the same instant are located between the stator poles. The rotor is situated between two stators composed of U-shaped laminated poles, and two ring coils placed inside each stator. The coil is suspended above the PMs to limit the negative flux leakage from the inactive magnets. The magnetic flux Ô is closed through the stator poles in the direction perpendicular to the rotor plane (Fig. 1 c). The density of this flux and the mesh of the model are depicted in Fig. 1 d). The design parameters of the TFM are listed in Table 1.
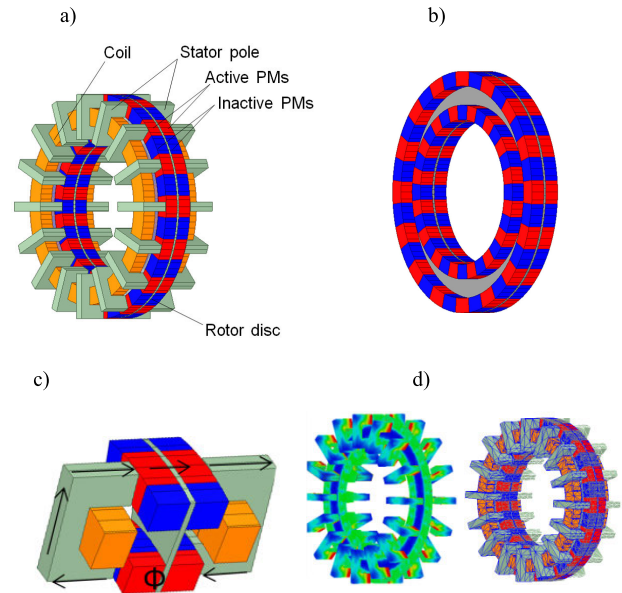

FIGURE 1. Electromagnetic model of the transverse-flux machine with double core: a) general view, b) rotor disc assembly, c) magnetic flux direction in the 1/16th of the model, d) magnetic flux density distribution in the machine.

TABLE 1. Design parameters of the TFM.

Parameter	Value
Geometry:	
Outer diameter, mm	500
Inner diameter, mm	300
Air-gap, mm	1
Number of poles	32
Permanent magnets:	
Material	Y40 (Strontium Ferrite $Sr_{0.6}Fe_2O_3$)
Residual flux density B_r, mT	450
Magnetic coercivity H_c, kA/m	266.6
Relative permeability μ_r	1.01
Stator poles:	
Material	Electric steel M19
Thickness, mm	0.23
Conductivity, S/m	2,000,000
Hysteresis core loss coefficient at 60 Hz k_h, W/m^3	17.02
Eddy current loss coefficient at 60 Hz k_e, W/m^3	0.43
Winding:	
Material	Copper
Conductivity, S/m	5,800,000
Number of winding turns	100
Winding filling factor	0.6
Cross-section area of the winding, mm²	1,200
Operation:	
Number of phases	1
Output Power, W	1,000
Speed, rpm	225
Frequency, Hz	60
Rated current, A	10
Ambient temperature	300 K

To research how the negative flux leakage of the inactive magnets influences the back EMF of the motor, the inactive
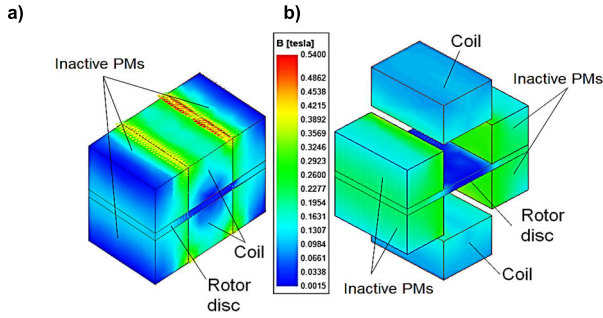
FIGURE 2. Results of the magnetostatic analysis of the transverse-flux machine (TFM): a) conventional TFM model with a coil placed on the rotor disc, b) TFM with suspended coil above the permanent magnets.
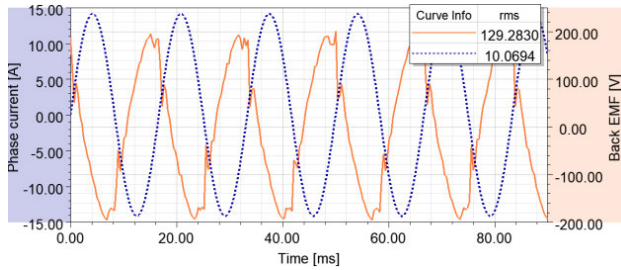

FIGURE 3. Transient characteristics of the transverse-flux machine at rated speed and current: a) back electromotive force with phase current, b) electromagnetic torque.

fragment of the machine is analyzed using magnetostatic analysis. This fragment involves a part of the coil between the stator poles with inactive magnets. The results of the analysis are illustrated in Fig. 2. The average negative flux density of the coil placed on the rotor disc is 0.18 T (Fig. 2 a), whereas the negative flux of the suspended coil (Fig. 2 b) is only 0.13 T. As a result of this improvement the TFM demonstrated 30% higher back EMF when compared to the conventional model.

The back EMF, phase current and electromagnetic torque of the motor are calculated using ANSYS® transient analysis, and illustrated in Fig. 3.

The positive and negative amplitudes of the back EMF are slightly different due to the small error in calculation associated with 3D FEM software. The phase shift between the back EMF (solid line) and phase current (dashed line on Fig. 3 a) is due to a high coil inductance, compared to other brushless DC motors. This is a common drawback of all the TFMs with ring coils, mainly caused by the coil regions located between the stator poles at a particular instant. Another well-known disadvantage of TFMs is high cogging torque which develops ripples of electromagnetic torque (Fig. 3 b). The ripples, however, can be mitigated by the mechanical skew between phases if a three-phase design is considered [18].

There are two major electromagnetic losses produced by the TFM: core losses and stranded (coil) losses. In the TFM discussed here, the core losses are generated in the stator poles, and the stranded loss is produced in the coil.
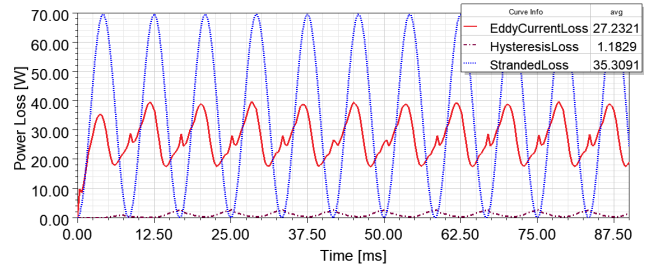

FIGURE 4. Core and coil (stranded) losses of the transverse-flux machine at rated speed and current.
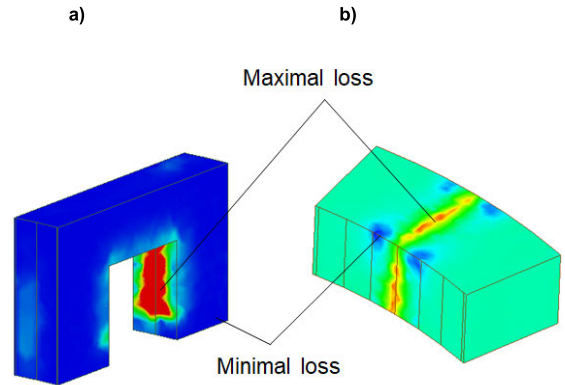

FIGURE 5. Volumetric losses in the transverse-flux machine elements: a) stator pole, b) 1/16th of the coil.

Core losses involve eddy current loss P_e, hysteresis loss P_h, and additional loss P_a:

$$P_{core} = P_e + P_h + P_a \qquad (1)$$

Eddy current loss is described by:

$$P_e = k_e B_m^2 f^2 \qquad (2)$$

where k_e – is the eddy current loss coefficient which depends on the lamination thickness d, and density of the laminated material ρ. B_m – is the magnetic flux density in the lamination, and f – is the electrical frequency. Eddy current loss coefficient is calculated as follows:

$$k_e = \pi^2 \cdot d^2 / (6 \cdot \rho) \qquad (3)$$

And the hysteresis loss:

$$P_h = k_h B_m^2 f \qquad (4)$$

where k_h – is the hysteresis loss coefficient.

The coefficient k_e and k_h are determined from the Eqs. 3 and 4 using the power loss values for steel M19 provided by the manufacturer. Additional loss P_a is a result of micro eddy currents generated by moving domain walls which are not included in this research.

The winding loss of the TFM is described as:

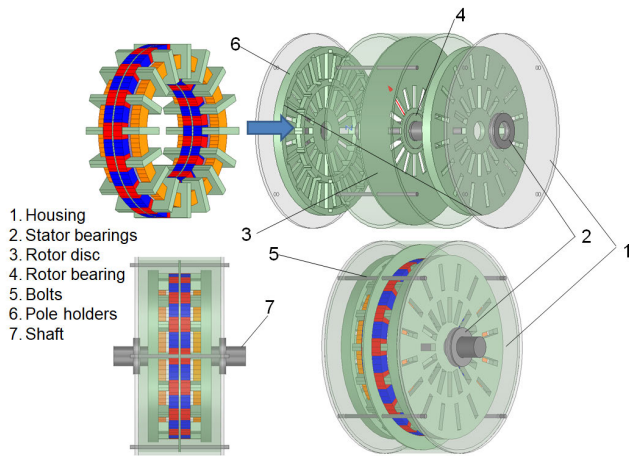$$P = \frac{1}{\sigma} \int J^2 dV \qquad (5)$$

FIGURE 6. Housing assembly of the transverse-flux machine.

FIGURE 7. 1/16th of the transverse-flux machine with ceramic elements placed in the hosing.

where σ – is electrical conductivity, J – is current density, and V – is the volume of the coil. The power losses of the machine at rated parameters are illustrated in Fig. 4.

The average value of the coil loss of the TFM is 35.3 W. The core loss which combines hysteresis and eddy current losses is 27.23 W. The ratio of the core and coil losses to the volume of the stator pole and coil determines the volumetric loss of these elements. The volumetric loss of the stator pole and coil are illustrated in Fig. 5.

The maximum value of the volumetric loss in the stator pole is 228 $^{kW}/_{m^3}$ (Fig. 5 a), and the same loss in the coil is 21.97$^{kW}/_{m^3}$ (Fig. 5 b). The minimal volumetric losses of the stator and coil are: 4 $^{W}/_{m^3}$, and 3.7 $^{W}/_{m^3}$ respectively. The volumetric losses will be mapped to the 3D FEM mechanical model of the motor to calculate temperature distribution in the machine.

III. THERMAL ANALYSIS

The temperature distribution in the motor depends on various factors including motor geometry, boundary conditions, thermal characteristic of the machine elements, and operational conditions of the motor.

A. MOTOR GEOMETRY

The assembly of the motor is explained in Fig. 6. The TFM is enclosed in the aluminum housing *1* mounted on the stator bearings *2*, whereas the rotor disc *3* is attached to the shaft trough the rotor bearing *4*. The bolts *5* tie the rotor disc to the housing at both ends. The stator poles are held by the pole holders *6*, which are firmly attached to the shaft *7*. In this design the coil is stationary with respect to stator poles, and it is the stator poles that rotate around the PMs and the coil. The openings in the rotor disc and pole holders are intended to reduce the machine's weight, and allow air circulation. The heat of the coil will be partially removed by rotating stator poles due to the air turbulence on the coil surface.

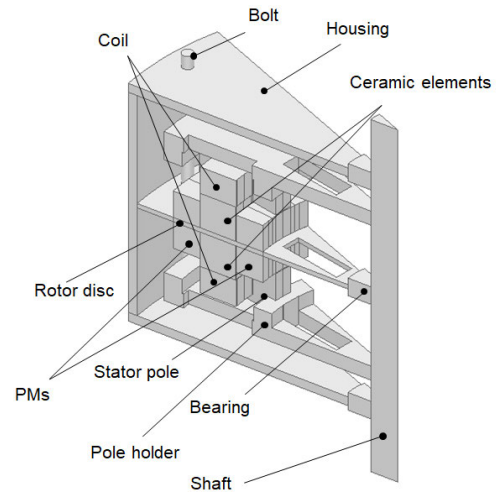Two ring-shaped ceramic elements are placed on the rotor disc as illustrated in Fig. 7. The coil is fixed to the ceramic elements with a thermally conductive adhesive. The coil and stator poles have 1 mm clearance to allow the motor rotation. The ceramic elements and the PMs have a clearance of 0.5 mm to account for thermal expansion and mechanical deformation of the PMs and ceramics during hard operating conditions. The advantage of the motor geometry is in simple maintenance. By disassembling housing on a particular motor side, and removing the pole holders with stator poles, the coil and the PMs of the motor can be accessed. To facilitate the cooling of the machine, a forced-air-cooling housing can be attached to one of the motor sides.

B. BOUNDARY CONDITIONS

The heat of the machine elements is transferred by convection and conduction until the steady-state is reached. Therefore, the following boundary conditions are specified in order to calculate the steady-state temperature distribution in the machine:

- Periodic boundary condition allows analyzing only 1/16th of the machine geometry as shown in Fig. 7.
- Convective heat transfer boundary is applied to the walls exposed to the free steam temperature of the air. The default temperature of the air is set to 300 K.
- Conduction boundary is applied to all touching walls of solid bodies.

The heat transfer by convection is described by the Newton's Law of cooling:

$$q = hA(T_w - T_\infty) \tag{6}$$

where:

$q-$ is heat transfer rate (W), h - is heat transfer coefficient (W/(m^{2}K)) T_w- is wall temperature (K), T_∞ - is free stream air temperature (K).

The heat transfer coefficient for air is set to 10 W/(m^{2}K) which is applicable for free convection analysis.

TABLE 2. Thermal characteristics of the transverse flux machine materials taken from ansys library.

Part	Material	Specific heat, J/(kg·K)	Thermal conductivity, W/(mK)
Casing	Aluminum	871	202.4
Pole holders, shaft, bearings, bolt	Carbon Steel	495.9	60.4
Rotor disc	Steel 904L	500	11.5
Stator poles	Electrical steel	502.48	16.3
Winding	Cooper	381	387.6
Permanent magnets	Ferrite	1,045	4.2
Ceramic elements:	Glass ceramic	869.99	2.5
	Aluminum oxide	772.09	13.7
	Silicon nitride	617.71	33

The heat transfer by conduction between two walls is described as:

$$q'' = -k \frac{(T_2 - T_1)}{L} \tag{7}$$

where:

$k-$ is the thermal conductivity of the materials (W/(m.K)), T_1 and T_2 – are the temperatures at the walls (K), and L - is the thickness of the element (m).

Specific heat is another important quantity that determines the thermal capacitance in the system. In other words, specific heat is the quantity of heat necessary to increase the temperature of one gram of a substance by 1 °C.

C. THERMAL PROPERTIES OF THE TRANSVERSE FLUX MACHINE ELEMENTS

Thermal conductivity of the materials used in the design and specific heat coefficients are listed in Table 2.

Silicon nitride is one of the most heat conductive ceramic elements with a thermal conductivity 13 times higher than that of glass ceramic, and 2.4 times higher than aluminum oxide. Silicon nitride conducts heat better than electrical steel, and the non-magnetic steel 904L used in the rotor disc. The specific heat coefficient of silicon nitride is lower than glass ceramic and aluminum oxide, which gives it the advantage of faster heat transfer in and out of the element.

D. OPERATIONAL CONDITIONS

The temperature distribution of the TFM is calculated when the motor operates at the rated speed, but at high load conditions when the phase current is 30, and 50 A. To observe the influence of the ceramic elements on the temperature distribution in the TFM, the temperature of the machine is compared with and without ceramic elements in Fig. 8.

When the machine has a 30 A current and is rotating at a speed of 300 rpm, the coil is the main source of heat according to the results presented in Fig. 8. In the model without the
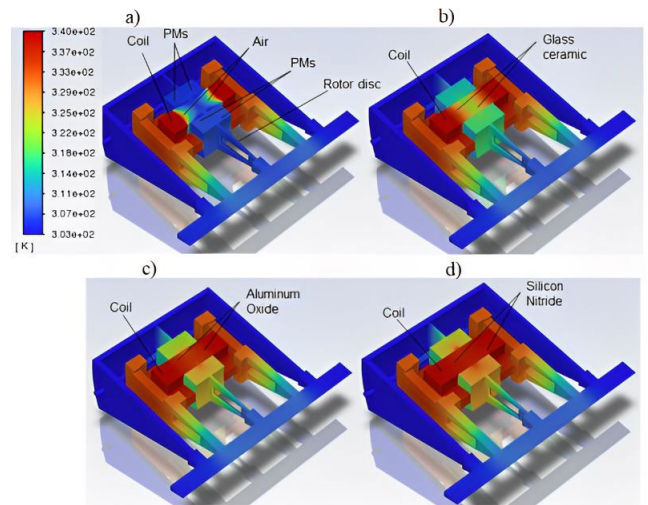

FIGURE 8. Temperature distribution in the transverse-flux machine at 30 A load current and rated speed of 300 rpm: a) machine without ceramic element, b) machine with glass ceramic element, c) machine with aluminum oxide ceramic element, d) machine with silicon nitride ceramic element.

TABLE 3. Temperature distribution in the coil and permanent magnets of the transverse-flux motor.

Ceramic Element	Air	Glass ceramic	Aluminum oxide	Silicon nitride
Temperature (K) At 30 A :				
Coil	334	328	325	324
PMs	304	312	315	318
Ceramic element	–	320	323	324
At 50 A :				
Coil	392	374	366	364
Permanent magnets	311	332	341	346
Ceramic element	–	344	354	360

ceramic element (Fig. 8 a), the coil heat is dissipated through the motor geometry only by convection because there are no contacts between the coil and other parts of the geometry. When the glass ceramic element is placed beneath the coil (Fig. 8 b), the heat flux of the coil is transferred to the ceramic element by conduction as described in Eq. 7. This results in a temperature drop in the coil. The heat of the ceramic elements is then transferred to the rotor disc, and from the rotor disc to the magnets. As a result, the magnets start warming as can been seen by comparing Figs. 8 a) and b). The higher the thermal conductivity of the ceramic element, the more heat is transferred to the magnets, and, consequently, the larger is the temperature drop in the motor coil. This is confirmed by analyzing the models with aluminum oxide and silicon nitride element (Fig. 8 c and d). Increasing the motor loading to 50 A - increases the heat transfer between the motor elements which results in a higher temperature drop in the coil. This can be observed in Table 3, where the temperatures of the coil, ceramic elements, and PMs are summarized. Thus, at a load current of 30 A the difference between the coil temperature without a ceramic element and with the silicon

TABLE 4. Mechanical properties of the ceramic elements taken from ANSYS library.

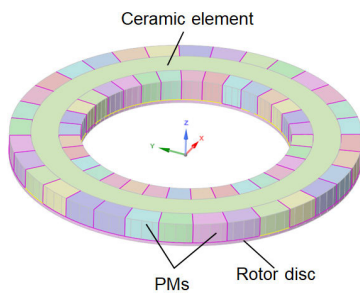| Material Parameter	Glass-ceramic	Aluminum oxide	Silicon nitride
Density, kg/m³	2,402	3,475	3,195
Young's modulus, Pa	$0.87 \cdot 10^{11}$	$2.45 \cdot 10^{11}$	$3.13 \cdot 10^{11}$
Thermal expansion coefficient, 1/°C	$1.039 \cdot 10^{-5}$	$8.1 \cdot 10^{-6}$	$5.4e \cdot 10^{-6}$
Tensile yield strength, MPa	123.2	200	500
Tensile ultimate strength, MPa	123.2	200	500
Strain, %	0.1	0.15	0.2

FIGURE 9. 3D FEM model of the rotor with the aluminum oxide ceramic element.

nitride element is 10 K. The same difference is 28 K when the machine operates at 50 A. This demonstrates the effectiveness of the ceramic elements at high motor loading.

If the temperature of the rotor is lower than the temperature of the coil, the heat transfer in the machine works backward, from the rotor disc to the ceramic element, and then to the coil. This scenario can also happen in the machine with rare-earth magnets. Operating at high speed and low load the rotor of the machine becomes a hot spot due to the eddy loss in rare-earth magnets. The heat transfer between the PMs, ceramic elements, and motor coil can prevent the irreversible demagnetization of the rare-earth magnet. Irreversible demagnetization of the rare-earth PMs starts at 80°C, - whereas this temperature for the FMs is 250 °C.

IV. STRUCTURAL ANALYSIS

The ceramic elements can expand or contract due to the temperature change depending on their thermal expansion coefficient provided in Table 4.

Thermal stress in the element is calculated by multiplying the change in temperature, the material's thermal expansion coefficient and the material's Young's modulus:

$$\sigma = E \cdot \alpha \cdot (T_f - T_0) \qquad (8)$$

where T_0 – is the initial temperature (300 K), and T_f – is the final temperature. E – is Young's modulus, and α – is thermal expansion coefficient.

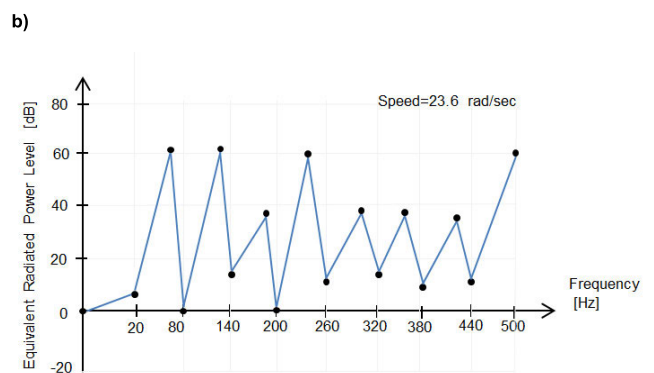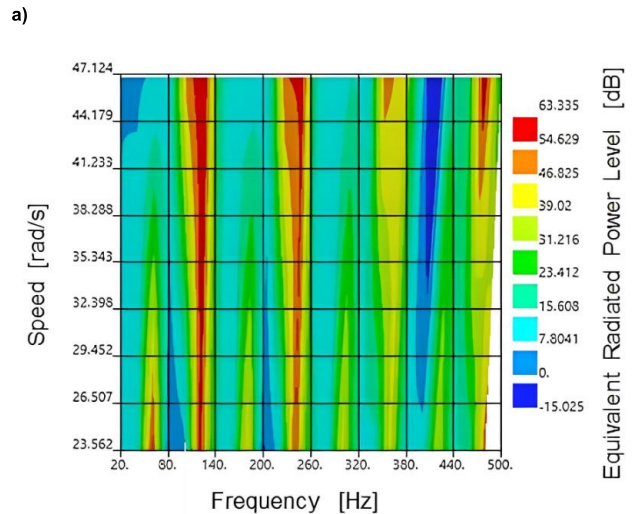The mechanical properties of the ceramic elements are listed in Table 4.

a)

b)

FIGURE 10. Equivalent Radiated Power Level (ERP) of the ceramic elements at various frequencies: a) Waterfall diagram of the motor vibrations at speed range between 23.6 rad/s to 47.01 rad/s, b) ERP at resonant frequencies.

The structural analysis of the rotor of the TFM with an aluminum oxide ceramic element is examined using a 3D FEM model shown in Fig. 9. The analysis is conducted the aluminum oxide temperatures are 354 K and 413 K. The calculated average thermal stress of the aluminum oxide at temperature 354 K is 105 MPa. If the temperature of the element is increased to 413 K the thermal stress increases to 240 MPa. This value will exceed the tensile yield strength of the aluminum oxide which is given in Table 4. Consequently, the material will fracture in this case.

The electromagnetic torque ripple discussed in Fig. 3 b) is a source of vibration. Caused by electromagnetic forces between the stator poles and PMs, the vibration can deform the ceramic material. In order to investigate the endurance of the ceramic elements to motor vibration, a harmonic analysis is conducted by mapping the electromagnetic solver to the modal mechanical solver in the 3D FEM. In this analysis, the machine is tested in a speed range of 23.6 rad/s to 47.01 rad/s. As a result, a waterfall diagram of the machine acoustics is obtained and can be seen in Fig. 10 a).
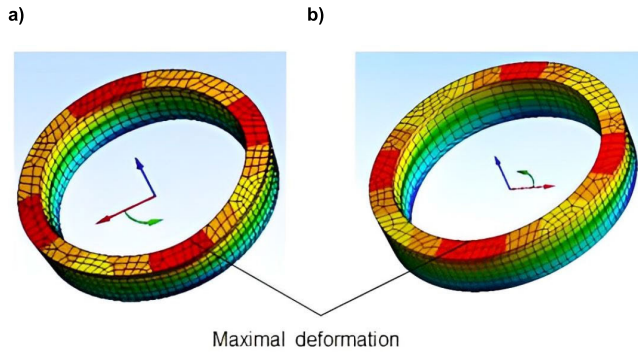
FIGURE 11. Deformation analysis of the ceramic elements at rated speed of the motor: a) glass ceramic, b) silicon nitride.

The diagram demonstrates maximal possible dynamic radiation of ceramic elements (Equivalent Radiated Power Level) for specific excitations in frequency. The acoustic noise (in dB), radiated by the machine is obtained from the vibration velocity of the ceramic elements. According to the diagram the ceramic element experiences vibrations of multiple frequencies ranging from 20 to 480 Hz. The resonant frequencies of the ceramic elements when the motor operates at a rated speed of 23.6 rad/sec are separately demonstrated in Fig. 10 b). The maximum noise level of the vibrations is 63 dB and occurs at frequencies of 60, 120, and 480 Hz.

These vibrations apply stress and cause radial deformation of the ceramic. The deformation analysis investigates the endurance of the glass ceramic and silicon nitride elements to the motor vibration. The results of the analysis are shown in Fig. 11. The maximal deformation length of the ceramic glass element is $0.1289 \cdot 10^{-3}$ mm, and for the silicon nitride element this value is $0.05882 \cdot 10^{-3}$ mm. Silicon nitride demonstrated better resistance to deformation if compared to glass ceramic due to its higher tensile ultimate strength. To verify whether the elements break at such deformation, the radial strain of the ceramic element can be determined by Eq. 9.

The strain is calculated as a ratio of the deformation lengths ΔL to the original length L of the element before the test.

$$\varepsilon = \frac{\Delta L}{L} \qquad (9)$$

The original radial length of the ceramic ring is 40 mm. Therefore:

strain of glass ceramic:

$$\varepsilon = \frac{\Delta L}{L} \cdot 100\% = \frac{0.1289 \cdot 10^{-3}}{40} \cdot 100\% = 0.322 \cdot 10^{-3}\%$$

strain of silicon nitride:

$$\varepsilon = \frac{\Delta L}{L} \cdot 100\% = \frac{0.05882 \cdot 10^{-3}}{40} \cdot 100\% = 0.147 \cdot 10^{-3}\%$$

The calculated strains of the ceramic elements are considerably lower if compared to the fracture strain in Table 4.

The motor elements such as permanent magnets, rotor core, stator poles, and coil can also deform under high temperatures, vibration, and external loads. This will provide
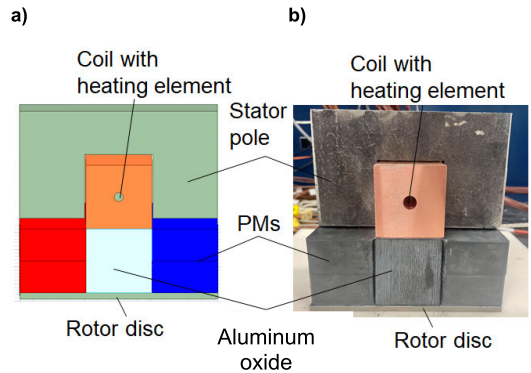

FIGURE 12. An experimental fragment of the TFM with double core: a) 3D FEM model, b) physical prototype.
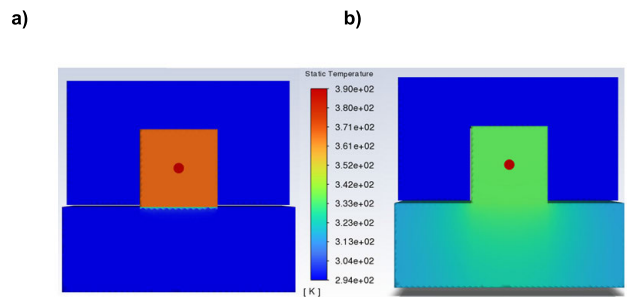

FIGURE 13. Thermal analysis of the experimental fragment of the TFM: a) TFM without ceramic element (air), b) TFM with aluminum oxide ceramic element.
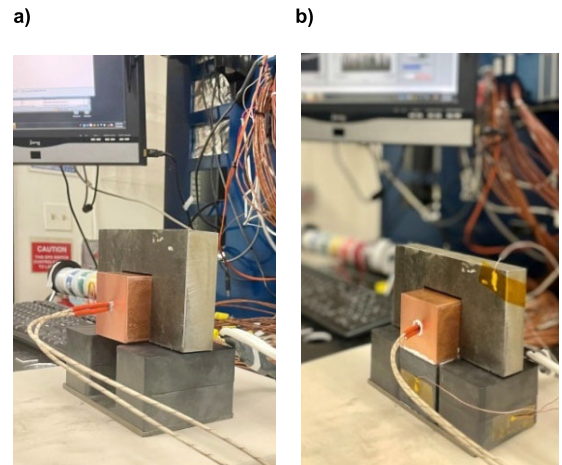

FIGURE 14. Thermal characterization of the physical section of the TFM: a) TFM without ceramic element (air), TFM with alumina oxide ceramic.

additional mutual tensile stresses on ceramic elements. If the ceramic element deforms during motor operation it can damage the ferrite magnets. Therefore, in this study the ceramic elements were placed on a small distance from the magnets. The ceramic elements are able to withstand severe thermal, mechanical and wear situations, and can be used in extremely demanding environments. These elements can replace expensive aluminum in motor cooling jackets and housing adding additional durability and strength to the motor structure.
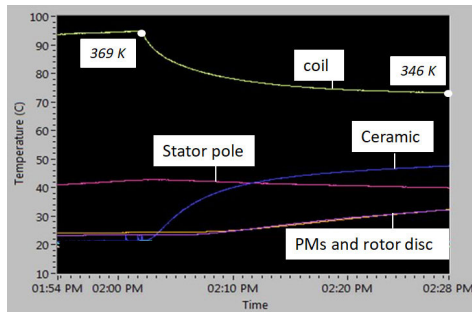
FIGURE 15. Temperature change in the transverse-flux machine after the aluminum oxide elements is slid beneath the coil.

TABLE 5. Results of the steady-state and thermal analysis of the transverse-flux motor.

Model	3D FEM	Physical
Average Temperature, K		
Without ceramic elements:		
Coil	372	369
Rotor disc	300	296
Permanent magnet	300	296
Stator pole	300	296
With ceramic elements:		
Coil	345	346
Ceramic element	322	325
Rotor disc	315	311
Permanent magnet	313	309
Stator pole	301	308

V. LABORATORY TEST

The laboratory experiment is conducted at the National Renewable Energy Laboratory on a rectangular section of the machine. Motor symmetry allows the analysis of only half of the machine. Therefore only a half of the 1/16th geometry of the motor was taken for the test. The geometry is transformed into the rectangular shape at which the original volumes of the section elements are maintained. The main goal of the experiment is to observe heat transfer from the coil to the rotor through the ceramic element. The other goal was to verify the accuracy of the mesh and boundary conditions of the computer models used in the study. To verify the accuracy of the computer model settings as mesh size and boundary conditions, the identical 3D FEM model of the motor was developed. The calculation and experimental results will be compared to find the error of the computer models used in the study. The computer model and the experimental fragment are shown in Fig. 12.

The heating element is placed inside the coil and heated to 390 K until steady-state temperature is reached in the machine. The air temperature is set to 295 K which corresponds to the temperature in the laboratory. The results of the computer simulation of the model without a ceramic element, and the model with aluminum oxide ceramic are shown in Fig. 13.

The temperature distribution in the motor elements is summarized in Table 5 and later will be compared with the physical model.

The evaluation of the physical model is conducted by attaching five T-type thermocouples (TCs) to the surfaces of the coil, stator pole, ceramic element, PMs, and rotor disc. The TCs were calibrated to an uncertainty of 0.05 $°C$. To increase the thermal conductivity between the TCs and the surfaces, thermo-paste was applied at the points of contacts. The TCs were connected to the data acquisition system and Lab View software to process the results. The heating element was connected to a 24 V DC power to generate heat of 390 K. The experimental physical models of the motor section with and without a ceramic element are shown in Fig. 14.

The temperature of the fragment parts recorded during the test is displayed in Fig. 16. At the beginning, the model was analyzed without the ceramic element, and the coil was suspended above the magnets by means of a small object with low thermal conductivity. When the coil temperature reached a steady-state of 369 K, the aluminum oxide was slid beneath the coil without turning off the heating element. As a result, the temperature of the coil and the stator pole started decreasing due to the heat conduction between the coil and ceramic element. The temperature of the rotor disc and the PMs started to increase as shown in Fig. 15. With presence of the ceramic element the coil temperature dropped by 25 K before it reached steady-state. The steady-state temperatures of the fragment parts recorded during the experiment are listed in Table 5.

The discrepancy between the results recorded in the laboratory and the results obtain during computer simulation does not exceed 5%. The error is explained by assuming zero thermal resistances between the touching elements in 3D FEM models. However, during the test, the thermal resistance was higher than zero due to the imperfection of the touching surfaces. Thermo-paste was applied between the touching elements to decrease the interface resistance to some level.

VI. CONCLUSION

The paper introduced a novel topology of electrical motor with ceramic elements for cooling and structural purposes. The electromagnetic and mechanical analyses, as well as an experimental test prove that ceramic materials can be successfully employed in the body of a TFM with double stator. Transferring heat from the hot to cold spots of the machines, the ceramic elements can become an important asset to electrical machines. The two goals of the research were reached: a) the ceramic elements decreased motor coil temperature, and b) suspending the coil above the PMs, the back EMF of the motor was increase by 30%. Printing the elements using 3D-printer can simplify the manufacturing process of the motors and generators. The results of structural analysis show the ceramic elements a durable and resistant to thermal and mechanical stresses confirming their applicability in electric machines. Ceramic materials can be easily machined with conventional metal cutting machinery. These factors make the ceramic compete against conventional aluminum and steel used in electrical motors and generators.

The laboratory test proved the accuracy of the computer model settings such as mesh size, and boundary conditions. The discrepancy between the computer and laboratory models was only 5%.

The future scope of study involves investigation of the use of ceramic cooling jackets for liquid cooling in high speed electrical machines.

The innovation demonstrated in this paper is also applicable to machines with rare-earth PMs. In this case the ceramic elements can transfer excessive heat from the PMs to the other parts of the machine and prevent irreversible demagnetization of the magnets.

REFERENCES

[1] M. Ahmad, D. Ishak, T. Leong, and M. Mohamed, "Analytical subdomain model for double-stator permanent magnet synchronous machine with surface-mounted radial magnetization," *Eng. Proc.*, vol. 12, no. 1, p. 37, 2021, doi: 10.3390/engproc2021012037.

[2] Z. Wang, B. Liu, L. Guan, Y. Zhang, M. Cheng, B. Zhang, and L. Xu, "A dual-channel magnetically integrated EV chargers based on double-stator-winding permanent-magnet synchronous machines," *IEEE Trans. Ind. Appl.*, vol. 55, no. 2, pp. 1941–1953, Mar. 2019.

[3] W. Gul, Q. Gao, and W. Lenwari, "Optimal design of a 5-MW double-stator single-rotor PMSG for offshore direct drive wind turbines," *IEEE Trans. Ind. Appl.*, vol. 56, no. 1, pp. 216–225, Jan. 2020.

[4] A. Mahmoudi, N. A. Rahim, and W. P. Hew, "Axial-flux permanent-magnet machine modeling, design, simulation and analysis," *Sci. Res. Essays*, vol. 6, no. 12, pp. 2525–2549, Jun. 2011, doi: 10.5897/SRE11.334.

[5] M. Kiani, W. Wang, L. Gu, and B. Fahimi, "PM-assist double stator synchronous machine," in *Proc. IEEE Int. Symp. Ind. Electron.*, vol. 7, Jun. 2017, pp. 342–347.

[6] S. Asgari and M. Mirsalim, "A novel dual-stator radial-flux machine with diametrically magnetized cylindrical permanent magnets," *IEEE Trans. Energy Convers.*, vol. 66, no. 5, pp. 3605–3614, May 2019, doi: 10.1109/TIE.2018.2856211.

[7] R. Zhu, C. Di, X. Bao, and J. Liu, "Influence of the slots number combinations among the inner and outer stator on torque ripple in dual-stator permanent magnet synchronous motors," in *Proc. 24th Int. Conf. Electr. Mach. Syst. (ICEMS)*, Oct. 2021, pp. 1137–1141.

[8] Y. Zhao, W. Huang, W. Jiang, X. Lin, and X. Wu, "A hybrid-slot radial-flux dual-stator permanent-magnet machine with fault-tolerant consideration," *IEEE Trans. Transport. Electrific.*, vol. 7, no. 1, pp. 214–224, Mar. 2021.

[9] J. Zhang, B. Zhang, G. Feng, and B. Gan, "Design and analysis of a low-speed and high-torque dual-stator permanent magnet motor with inner enhanced torque," *IEEE Access*, vol. 8, pp. 182984–182995, 2020.

[10] Y. Zhao, W. Huang, W. Jiang, X. Lin, and D. Dong, "Optimal design of double stator permanent magnet motors used in electric vehicle," in *Proc. 22nd Int. Conf. Electr. Mach. Syst. (ICEMS)*, Aug. 2019, pp. 1–4.

[11] L. Mo, T. Zhang, X. Liu, X. Zhang, and Y. Tao, "Lumped-parameter thermal model for a double-rotor flux-switching permanent-magnet machine," in *Proc. IEEE Int. Conf. Appl. Supercond. Electromagn. Devices (ASEMD)*, Apr. 2018, pp. 1–2, doi: 10.1109/ASEMD.2018.8558958.

[12] A. Parsapour, M. Moallem, I. Boldea, and B. Fahimi, "High torque density double stator permanent magnet electric machine," in *Proc. IEEE Int. Electric Mach. Drives Conf. (IEMDC)*, May 2019, pp. 664–670, doi: 10.1109/IEMDC.2019.8785192.

[13] Z. Wan, A. Ahmed, I. Husain, and E. Muljadi, "A novel transverse flux machine for vehicle traction applications," in *Proc. IEEE Power Energy Soc. Gen. Meeting*, Denver, CO, USA, Jul. 2015, pp. 1–5.

[14] O. Dobzhanskyi and R. Gouws, "Performance analysis of a permanent magnet transverse flux generator with double coil," *IEEE Trans. Magn.*, vol. 52, no. 1, pp. 1–11, Jan. 2016.

[15] Z. Jia, H. Lin, S. Fang, and Y. Huang, "A novel transverse flux permanent magnet generator with double C-Hoop stator and flux-concentrated rotor," *IEEE Trans. Magn.*, vol. 51, no. 11, pp. 1–4, Nov. 2015, doi: 10.1109/TMAG.2015.2452913.

[16] O. Dobzhanskyi and E. E. Mendrela, "Performance of a 3-phase permanent magnet transverse flux wind power generator with internal stator," in *Proc. IEEE Green Technol. Conf. (IEEE-Green)*, Baton Rouge, LA, USA, Apr. 2011, pp. 1–5.

[17] O. Dobzhanskyi, E. E. Mendrela, and A. M. Trzynadlowski, "Analysis of leakage flux losses in the transverse flux permanent magnet generator," in *Proc. IEEE Green Technol. Conf. (IEEE-Green)*, Baton Rouge, LA, USA, Apr. 2011, pp. 1–6.

[18] O. Dobzhanskyi, R. Gouws, and E. Amiri, "Optimal switching-flux motor design and its cogging effect reduction," in *Proc. IEEE 58th Int. Sci. Conf. Power Electr. Eng. Riga Tech. Univ. (RTUCON)*, Oct. 2017, pp. 1–9.

[19] D. Cozonac, S. Babicz, S. Ait-Amar-Djennad, G. Velu, A. Cavalini, and P. Wang, "Study on ceramic insulation wires for motor windings at high-temperature," in *Proc. IEEE Conf. Electr. Insul. Dielectr. Phenomena (CEIDP)*, Oct. 2014, pp. 172–175, doi: 10.1109/CEIDP.2014.6995757.

[20] O. V. Tikhonova, I. V. Malygin, S. L. Kulakov, and A. T. Plastun, "Analysis of the electromagnetic parameters of an induction motor with ring windings with ceramic insulation," in *Proc. Conf. Russian Young Researchers Electr. Electron. Eng. (ElConRus)*, Jan. 2022, pp. 1280–1283, doi: 10.1109/ElConRus54750.2022.9755498.

[21] E. Gundabattini and A. Mystkowski, "Review of air-cooling strategies, combinations and thermal analysis (experimental and analytical) of a permanent magnet synchronous motor," *Proc. Inst. Mech. Eng. C, J. Mech. Eng. Sci.*, vol. 236, no. 1, pp. 655–668, Jan. 2022, doi: 10.1177/0954406220987267.

OLEKSANDR DOBZHANSKYI received the Ph.D. degree in electrical engineering from Louisiana State University, Baton Rouge, LA, USA, in 2012. He is currently an Assistant Professor of electrical engineering with Point Park University, Pittsburgh, PA, USA. His research interests include design and analysis of rare-earth material-free electric machines, wave and wind energy conversion systems, and hybrid electric vehicles.

RUPERT GOUWS (Member, IEEE) received the Ph.D. degree in electrical and electronic engineering from North-West University, Potchefstroom, South Africa. He consulted for a variety of industry and public sectors in South Africa and other countries in the fields of energy engineering and energy management. He is currently a Professor specializing in energy management, electrical machines, and energy storage with North-West University. He is also Registered Professional Engineer with the Engineering Council of South Africa and a Certified Measurement and Verification Professional with the Association of Energy Engineers.

KEVIN BENNION received the B.Sc. degree in mechanical engineering from Brigham Young University, Provo, UT, USA, and the M.Sc. degree in mechanical engineering from the Rensselaer Polytechnic Institute. He was a Senior Research Engineer at the Advanced Power Electronics and Electric Machines (APEEM) Group, Center of Integrated Mobility Sciences, National Renewable Energy Laboratory (NREL). He came to NREL from Ford Motor Company, where he worked on powertrain systems and controls, including electric drive components for hybrid electric vehicles. He led research projects with DOE and industry focused on thermal management of power electronics and electric motors. He also supported research projects related to high power charging, vehicle thermal management, and vehicle systems analysis.

BIDZINA KEKELIA (Member, IEEE) received the bachelor's degree (Hons.) in mechanical engineering from Georgian Technical University, in 1992, the M.S. degree in renewable energy (solar thermal and PV) from the University of Oldenburg, in 1999, and the Ph.D. degree in mechanical engineering from The University of Utah, in 2012. He worked as a Postdoctoral Research Associate at The University of Utah, developing thermal battery prototypes for electric vehicles. Since 2015, he has been a Senior Research Engineer with the Advanced Power Electronics and Electric Machines (APEEM) Group, Center of Integrated Mobility Sciences, National Renewable Energy Laboratory (NREL). His research interest includes vehicle thermal management, exploring novel cooling methods for power electronics and electric traction drives for ground vehicles and electrified aviation.

J. TOMERLIN, photograph and biography not available at the time of publication.

E. COUSINEAU, (Member, IEEE) photograph and biography not available at the time of publication.

SREEKANT NARUMANCHI (Senior Member, IEEE) received the B.Tech. degree in mechanical engineering from IIT Kanpur, India, in 1997, the M.S. degree in mechanical engineering from Washington State University, Pullman, WA, USA, in 1999, and the Ph.D. degree in mechanical engineering from Carnegie Mellon University, Pittsburgh, PA, USA, in 2003. He is currently the Group Manager with the Center of Integrated Mobility Sciences, Advanced Power Electronics and Electric Machines (APEEM) Group, National Renewable Energy Laboratory (NREL), Golden, CO, USA. He leads a group of 14 researchers focused on thermal, electro-thermal, thermal-fluids, thermo-mechanical, and reliability aspects of power electronics and electric machines. He has authored or coauthored more than 95 peer-reviewed journals and conference papers and book chapters. His research interests include heat transfer, power electronics, electric machines thermal management, packaging, and reliability. He was a recipient of the Best Paper Award from the *ASME Journal of Electronic Packaging* in 2003, the ASME 2013 InterPACK Conference Outstanding Paper Award, the 2016 Research and Development 100 Award, and the 2018 ASME EPPD-K16 Clock Award. From 2020 to 2021, he was also a recipient of an Associate Editor of the Year Award from the *ASME Journal of Electronic Packaging*, the 2021 United States Council for Automotive Research Team Award, and the 2022 THERMI Award from the Semi-therm Educational Foundation. He is a part of the Executive Committee of the ASME Electronic and Photonic Packaging Division. He serves on advisory boards and a reviewer for numerous journals and federal agencies. He is an Active Associate Editor of the *ASME Journal of Electronic Packaging* and the IEEE Transactions on Components, Packaging, and Manufacturing Technology journal.

• • •